Study of Topological Weyl Points In Metamaterials

Guilherme Ruivo Lopes da Fonseca

***Abstract*—In this work we study two topological photonic systems: a reciprocal chiral metamaterial consisting of an array of metal wires in the shape of elliptical helices; and a magnetized plasma which is a naturally existing continuous medium. Both of these structures display Weyl points which are topological band degeneracies in 3 dimensions that arise at the linear crossing between longitudinal plasmonic modes and transverse modes. First, we analyse how nonlocality, a phenomenon present in these materials, affects the emergence of these three-dimensional linear degeneracies. Next, the topological properties of the magnetized plasma are characterized by a first principles method. Specifically, a photonic Green's function formalism is used in order to study the influence of Weyl degeneracies on the topology in 3-dimensional wave vector space and we calculate their topological charge. We apply two different regularization procedures in order to obtain well-defined topological invariants: introducing the effects of charge diffusion due to electron-electron repulsive interactions; and the application of a full wave vector cut-off. With our approach, we are able to compute the topological charge of Weyl points in metamaterials with in a computationally efficient way.**

***Index Terms*—Metamaterials, Helical Metamaterial, Band Structures, Weyl Points, Chern Number, Topological Photonics**

I. Introduction

Topological photonics has attracted much attention due to the prediction of topologically protected edge states that propagate without backscattering, enabling the flow of light immune to disorder and imperfections such as sharp bends or corners [1]–[3]. These chiral edge states are predicted by a topological invariant called the gap Chern number [4]. This is an integer number and it is by definition given by the sum of the individual Chern numbers of each set of bands below the specific band gap. Additionally, the bulk-edge correspondence principle [5], [6] states that when two topologically inequivalent photonic systems share a common band gap, the number of edge modes supported at an interface between them is given by the difference of the gap Chern numbers.

The standard theory used to calculate these topological invariants requires the Berry curvature which depends on the normal modes of the system [7]. However, the formalism that will be adopted for this work makes explicit use of the photonic Green's function which is also linked with the Chern invariants [8], [9], and it is more computationally efficient. Specifically, the gap Chern number is given by an integral of the photonic Green's function along a line of the complex frequency plane parallel to the imaginary axis. The line crosses the real frequency axis on a chosen value ω'_{gap} and this value should be confined between the lower and upper limits of the respective band gap in the real frequency axis. The first principles Green's function formalism is described by:

$$\mathcal{C}_{gap} = \frac{1}{(2\pi)^2} \iint_{BZ} d^2\mathbf{k} \int_{\omega'_{gap}-i\infty}^{\omega'_{gap}+i\infty} d\omega Tr\{\partial_1 \mathcal{G}_{\mathbf{k}}^{-1} \cdot \mathcal{G}_{\mathbf{k}} \cdot \partial_2 \mathcal{G}_{\mathbf{k}}^{-1} \cdot \partial_\omega \mathcal{G}_{\mathbf{k}}\}, \tag{1}$$

where Tr is the trace operator, ∂_ω=$\partial/\partial\omega$ and $\partial_j \mathcal{G}_{\mathbf{k}}^{-1} = \partial \mathcal{G}_{\mathbf{k}}^{-1}/\partial \mathbf{k}_j$ for $j = \{1, 2\}$ with $k_1 = k_x$ and $k_2 = k_y$.

It is possible to topologically classify continuous media, with no intrinsic periodicity, i.e with an underlying wave vector space that is an unbounded open region as was shown by M. G. Silveirinha [10]. However, a physical regularization procedure must be applied to the material response in order to overcome the problem of an ill-defined topology, i.e. non-integer Chern numbers. A general solution to guarantee a well-defined topology of a continuous system is to apply a full wave vector cut-off which acts by suppressing the nonreciprocal part of the material response, for large wave vectors.

The Chern invariants that relate to the existence of edge states along one-dimensional boundaries are defined over a 2-dimensional wave vector space, but there exists a 3-dimensional topological phase described by the number of Weyl points [11]–[16]. These physical entities are singular points that emerge as linear crossings between two topologically inequivalent bands. They are monopoles of the Berry curvature and come in pairs in symmetric points of momentum space with opposite charge. Importantly, they only emerge in systems with a broken time-reversal symmetry, a broken inversion symmetry or both. It is only possible to remove them by annihilating both points that make up one pair with each other, thus leading to robust topological surface states, often called photonic Fermi arcs [3].

There are two types of Weyl points. Type-I and type-II, both being topologically nontrivial, but exhibiting different physical properties. The isofrequency surface around a type-I Weyl point is an ellipsoid, hence these are also referred as elliptical Weyl points. In the case of the type-II Weyl point, the isofrequency surface is a hyperboloid, thus these are called hyperbolic Weyl points [12].

Firstly, in this work we study two photonic systems that display Weyl points: the helical metamaterial which is studied in section II; and a magnetized plasma which will is studied in section III. In section IV we apply the Green's function formalism to topologically characterize two nonlocal models of a magnetized plasma. Finally, In section V we derive the main conclusions from this work.

II. Helical Metamaterial

The first structure under study is a metamaterial consisting of an array of infinitely long wires shaped like elliptical helices, made from perfectly electrical conductors (PEC) and embedded in air. Its physical realization exhibits type-II Weyl points due to its nonlocal response, as it will be shown. Its geometry can be visualized in Fig. 1.

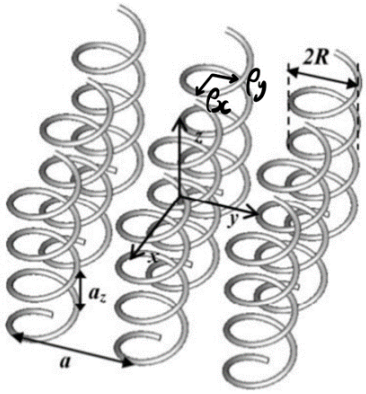

Fig. 1. Helical metamaterial - geometry and orientation. Picture taken from [17]

Metamaterials can be regarded as continuous media if the inclusions that constitute the unit cell are electrically small, i.e. their dimension is much smaller than the wavelength of the electromagnetic wave in the specific direction of propagation. In this situation they can be described by effective constitutive parameters which correspond to a homogenized model [18]–[20].

Before we analyse the dispersion of electromagnetic waves in a possible physical realization of this metamaterial, we will focus on the class of materials where the homogenized model of the helical metamaterial belongs to. We start with a bianisotropic homogeneous medium that possesses no spatial dispersion. The bianisotropy is due to chiral coupling (γ) between electric and magnetic fields and because the components of the permittivity and permeability tensors are all different. This type of media is described by the following constitutive relations:

$$\begin{pmatrix} \mathbf{D} \\ \mathbf{B} \end{pmatrix} = \begin{pmatrix} \overline{\epsilon} & i\sqrt{\epsilon_0\mu_0}\overline{\gamma} \\ -i\sqrt{\epsilon_0\mu_0}\overline{\gamma} & \overline{\mu} \end{pmatrix} \begin{pmatrix} \mathbf{E} \\ \mathbf{H} \end{pmatrix} \tag{2}$$

The only nonvanishing component of $\overline{\gamma}$ is $\gamma_{zz} = \gamma$ and the permittivity and permeability tensors are as follows [12]:

$$\frac{\overline{\epsilon}}{\epsilon_0} = \begin{bmatrix} \epsilon_x & 0 & 0 \\ 0 & \epsilon_y & 0 \\ 0 & 0 & \epsilon_z \end{bmatrix}, \quad \frac{\overline{\mu}}{\mu_0} = \begin{bmatrix} \mu_t & 0 & 0 \\ 0 & \mu_t & 0 \\ 0 & 0 & \mu_z \end{bmatrix}, \tag{3}$$

$$\epsilon_z = 1 - \frac{\omega_p^2}{\omega^2}. \tag{4}$$

As a first approximation, we consider ϵ_z to be the only dispersive constitutive parameter. It is characterized by Drude's dispersion and ω_p is a resonance frequency, also known as plasma frequency. This parameter is related to the geometry of the metamaterial as will be shown.

As we will see, the Weyl points arise along the k_z axis in the wave vector space, so we will focus mainly on propagation along the $\hat{\mathbf{z}}$ direction. The system supports three propagating modes, two of them transverse and one longitudinal. The transverse modes' dispersion relations are given by

$$\omega = \pm ck_z/\sqrt{\mu_t\epsilon_x}, \qquad \omega = \pm ck_z/\sqrt{\mu_t\epsilon_y}, \tag{5}$$

and so they are only degenerate when $\epsilon_x = \epsilon_y$. The longitudinal mode's dispersion relation is given by the solution to the equation $\epsilon_z - \gamma^2/\mu_z = 0$. It is a flat mode whose frequency is fixed at

$$\omega = \pm\omega_p/\sqrt{1 - \frac{\gamma^2}{\mu_z}} = \pm\omega_p', \tag{6}$$

independently of k_z. The Weyl points in this system arise as crossings between this flat longitudinal mode and the transverse modes. They have been shown to be indeed Weyl crossings [12], because they are twofold degenerate (not three) due to the anisotropy of the permittivity in the $\hat{\mathbf{x}}$ and $\hat{\mathbf{y}}$ directions, and because they are linear in all directions due to the chiral coupling. Without the chiral coupling, the dispersion in the $\hat{\mathbf{y}}$ direction is quadratic.

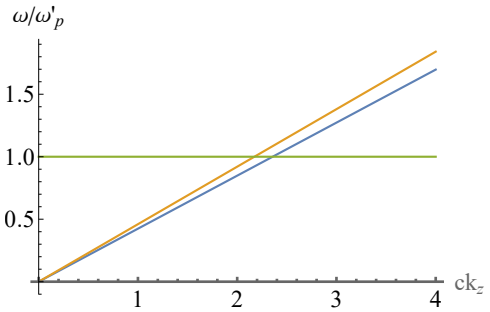

Fig. 2. Dispersion along the k_z axis. Crossings between longitudinal mode (green) and transverse modes (blue and yellow) are Weyl points. The parameters used here were $\omega_p = 1, \epsilon_x = 2, \epsilon_y = 1.7, \mu_t = 1, \mu_z = 1, \gamma = 0.8$.

The Weyl points displayed in Fig. 2 are at the boundary separating type-I and type-II. To achieve either one, nonlocality must be introduced. Nonlocality or spatial dispersion occurs when a medium's constitutive parameters depend on the wave vector component of the propagating electromagnetic wave. Metamaterials are known to exhibit this nonlocal effect [21], hence we will now consider a different ϵ_z [12] that models spatial dispersion:

$$\epsilon_z = 1 - \frac{\omega_p'^2}{\omega^2} + \frac{\gamma^2}{\mu_z} + \alpha k_z^2 \tag{7}$$

The nonlocality affects the longitudinal mode's dispersion by introducing a curvature or concavity that either tilts it up or down. The alpha parameter controls this tilt and thus the type

of Weyl point generated in the crossing. Recalling that this mode's dispersion is the solution to the equation $\epsilon_z - \gamma^2/\mu_z = 0$:

$$\omega = \pm \frac{\omega_p'}{\sqrt{1 + \alpha k_z^2}} \tag{8}$$

By analysing the second derivative of Eq. 8 with respect to the wave vector, it can be seen that is is positive for $\alpha < 0$ and negative for $\alpha > 0$ which means that with the first condition we have an upwards concavity and a downward concavity for the second one. Since in the plots of Fig. 3 there

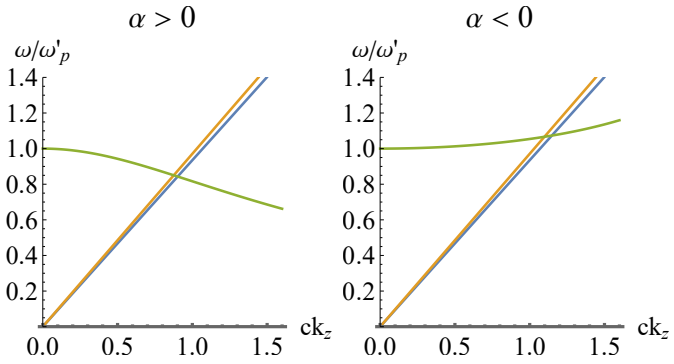

Fig. 3. Dispersion along the k_z axis with a nonlocal ϵ_z. The parameters used on both plots were $\omega_p' = 1, \epsilon_x = 2, \epsilon_y = 1.7, \mu_t = 1, \mu_z = 1$. For the plot on the left: $\alpha = 0.5, \gamma = 1$ and for the plot on the right: $\alpha = -0.1, \gamma = 0.71$.

are two degeneracies, we need to distinguish them. We will denominate the crossing between the yellow transverse mode and the green longitudinal mode as the first or inner Weyl point and the one between the blue and green modes as the second or outer Weyl point. By plotting the dispersion curves around one of the Weyl crossings, for example the second one, the conclusion can be derived that for $\alpha > 0$, the equifrequency curves are elliptical, signifying that it is type-I, as seen in Fig.4. On the other hand, for $\alpha < 0$, the equifrequency curves become hyperbolic, hence it becomes type-II, as seen inf Fig.5.

As we will see, for a physical realization of this metamaterial, it is only possible to obtain type-II Weyl points.

We will provide the link between the nonlocal bianisotropic model described previously and the effective medium theory of this metamaterial that is described in [17] and expanded in [12] to include ellipticity. This homogenization provides significant information about the physical realization of this metamaterial, specifically about its geometry. For example, the fact that this metamaterial's unit cell is an elliptical helix is the reason the values for ϵ_x and ϵ_y differ and consequently originate two non degenerate transverse modes, for propagation along the k_z axis. There is also an effective chirality due to lack of inversion symmetry of the helix (broken inversion symmetry). From the effective parameter formulae, we have:

$$\epsilon_z = 1 - \frac{1}{\beta^2/\beta_{p1}^2 - k_z^2/\beta_{p2}^2} + \frac{\gamma^2}{\mu_z}, \tag{9}$$

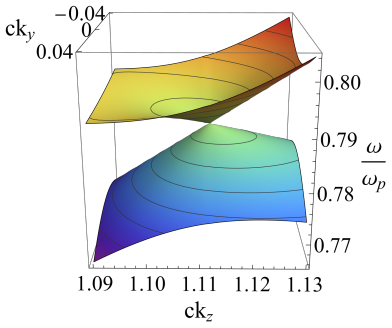

Fig. 4. Dispersion around second Weyl point with $\alpha > 0$ in $\hat{z}$ and $\hat{y}$. The parameters used here were $\alpha = 0.5, \gamma = 1, \omega_p' = 1, \epsilon_x = 2, \epsilon_y = 1.7, \mu_t = 1, \mu_z = 1$.

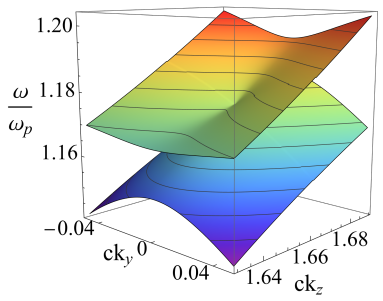

Fig. 5. Dispersion around second Weyl point with $\alpha < 0$ in $\hat{z}$ and $\hat{y}$. The parameters used here were $\alpha = -0.1, \gamma = 0.71, \omega_p' = 1, \epsilon_x = 2, \epsilon_y = 1.7, \mu_t = 1, \mu_z = 1$.

where $\beta = \omega/c$ is frequency normalized to speed of light in the vacuum, β_{p1} and β_{p2} are positive real-valued frequency independent parameters that depend only on the unit cell's geometry and lattice constant. We approximate the middle term of ϵ_z as:

$$\frac{1}{\frac{\beta^2}{\beta_{p1}^2} - \frac{k_z^2}{\beta_{p2}^2}} \approx \frac{1}{\beta^2/\beta_{p1}^2}\left(1 + \frac{\beta_{p1}^2}{\beta^2}\frac{k_z^2}{\beta_{p2}^2}\right), \quad \frac{\beta_{p1}}{\beta_{p2}}\left|\frac{k_z}{\beta}\right| < 1. \tag{10}$$

The nonlocal permittivity model in Eq. (7) is the effective permittivity ϵ_z in (9) with γ and μ_z given by the effective medium formulas in [17]. The leftover constants ω_p' and α are given by:

$$\begin{aligned} \omega_p' &= c\beta_{p1} \\ \alpha &= -\frac{\beta_{p1}^4}{\beta_{p2}^2 \beta^4} \end{aligned} \tag{11}$$

With this, we show that the alpha parameter is indeed negative, and so we conclude that this metamaterial possesses hyperbolic or type-II Weyl points.

III. Magnetized Plasma

In this section we analyse the dispersion relation for one local model and two nonlocal models of a magnetized plasma.

A. Local Model

A plasma is an isotropic medium that is parameterized by its plasma frequency which is defined by the volume density of the electrons N, their effective mass m, their charge $q = -e = 1.6 \times 10^{-19} C$ and the vacuum's permittivity ϵ_0:

$$\omega_p = \sqrt{\frac{Nq^2}{m\epsilon_0}}. \tag{12}$$

When an external DC (direct current, or static) magnetic field $\mathbf{B}_0$ is applied to the plasma medium, it becomes anisotropic. The field's effect is represented in the permittivity tensor through the cyclotron frequency. This is the angular frequency with which a free electron describes a circular cyclotron orbit, when it is under the influence of the magnetic field and is defined as:

$$\omega_c = -qB_0/m, \tag{13}$$

Throughout this work, the application of $\mathbf{B}_0$ is assumed to be in the $\hat{z}$ direction with positive orientation.

The permittivity tensor is an antisymmetric matrix with a gyrotropic structure [20]:

$$\overline{\epsilon} = \begin{bmatrix} \epsilon_t & -i\epsilon_g & 0 \\ i\epsilon_g & \epsilon_t & 0 \\ 0 & 0 & \epsilon_z \end{bmatrix}, \tag{14}$$

where each entry is

$$\epsilon_t = \epsilon_0 \left[1 - \frac{\omega_p^2}{\omega^2 - \omega_c^2}\right], \quad \epsilon_g = \epsilon_0 \left[\frac{-\omega_c \omega_p^2}{\omega(\omega^2 - \omega_c^2)}\right], \tag{15}$$

and

$$\epsilon_z = \epsilon_0 \left[1 - \frac{\omega_p^2}{\omega^2}\right]. \tag{16}$$

Since (14) is not symmetric $\overline{\epsilon} \neq \overline{\epsilon}^T$, this medium has a nonreciprocal response. The application of the bias field also breaks time reversal symmetry. Because we are considering a lossless case, these two notions are equivalent [10]. Furthermore, we will consider a nonmagnetic response $\overline{\mu} = \mathbb{1}$, where $\mathbb{1}$ is the identity matrix, and trivial magnetoelectric coupling $\overline{\xi} = \overline{\zeta} = 0$. Since the system's material matrix does not depend on the wave vector then this is a local model.

Our next objective is to obtain the dispersion characteristics of the bulk modes. This is possible by simply deriving the wave equation from Maxwell's equations (without a source), assuming a harmonic spatial and time variation of the type $e^{i(\mathbf{k}\cdot\mathbf{r} - \omega t)}$:

$$\mathbf{k} \times (\mathbf{k} \times \underline{\mathbf{E}}) + \frac{\omega^2}{c^2} \overline{\epsilon} \cdot \underline{\mathbf{E}} = 0 \tag{17}$$

The wave vector of the solution for Eq. 17 satisfies the dispersion relation [22]:

$$\left(\epsilon_t^2 - \epsilon_g^2\right) \epsilon_z \frac{\omega^4}{c^4} - \left(\left[\epsilon_t \left(\epsilon_t + \epsilon_z\right) - \epsilon_g^2\right] k_t^2 + 2\epsilon_t \epsilon_z k_z^2\right) \frac{\omega^2}{c^2} + \left(\epsilon_t k_t^2 + \epsilon_z k_z^2\right)\left(k_t^2 + k_z^2\right) = 0, \tag{18}$$

where $k_t = \|\mathbf{k_t}\| = \|k_x \hat{\mathbf{x}} + k_y \hat{\mathbf{y}}\|$, with subscript t representing wave vector components that are orthogonal to the static magnetic field.

As previously stated, the magnetized plasma presents photonic Weyl degeneracies, otherwise known as Weyl points. Due to the direction of $\mathbf{B}_0$, these appear along the k_z axis, i.e. only for wave vectors $\mathbf{k} = (0, 0, k_z)$. Along this axis there are straight horizontal bands at $\omega = \pm\omega_p$ which are longitudinal bulk plasmon modes that occur for $\epsilon_z = 0$. The Weyl points arise as crossings between this plasmon mode and transverse modes and the location of these linear degeneracies in wave vector space is given by [13]:

$$k_z^{Weyl} = \pm \frac{\omega_p}{c} \sqrt{\frac{\omega_c}{\omega_c \pm \omega_p}} \tag{19}$$

By fixing the plasma frequency ω_p and varying the cyclotron frequency ω_c, we vary the number of Weyl crossings:

- $\omega_c < \omega_p$: 1 pair of Weyl points in momentum space;
- $\omega_c > \omega_p$: 2 pairs of Weyl points in momentum space;

The dispersion diagrams for modes propagating in the direction of the applied static magnetic field are shown in Fig. 6, for the regime $\omega_c < \omega_p$ and for $\omega_c > \omega_p$. We can observe that the number of crossings between the longitudinal (in red) and the transverse (in blue) modes is indeed different between the two cases: while there are 4 crossings in the left panel, the right one shows 8. When $\omega_c = \omega_p$ the outer Weyl points go to infinity and for $\omega_c < \omega_p$ they are purely imaginary and so, in these conditions, only the inner Weyl points appear. For propagation in the xoy plane, hence for a wave vector

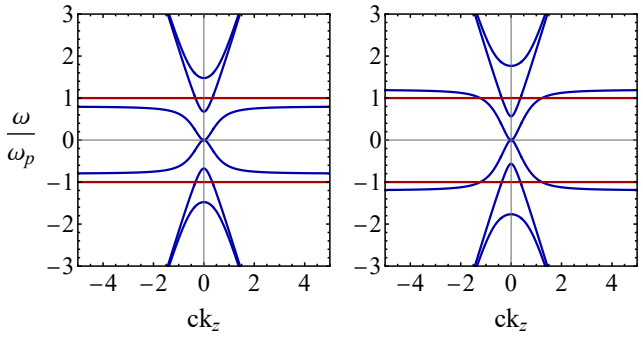

Fig. 6. Dispersion characteristics in the k_z axis for $\omega_c = 0.8\omega_p$ on the left, $\omega_c = 1.2\omega_p$ on the right and $\omega_p = 0.5c$ in both plots. The longitudinal mode is highlighted in red.

$\mathbf{k} = (k_x, ky, 0)$, the plane waves supported by the medium decouple into transverse electric (TE) waves ($E_z \neq 0$ and $H_z = 0$) and transverse magnetic (TM) waves ($H_z \neq 0$ and

$E_z = 0$). The dispersion relations for these photonic modes are, respectively:

$$k^2 = \epsilon_z \left(\frac{\omega}{c}\right)^2, \quad \text{TE modes,} \tag{20}$$

$$k^2 = \epsilon_{ef} \left(\frac{\omega}{c}\right)^2 \Leftrightarrow k^2 = \frac{\epsilon_t^2 - \epsilon_g^2}{\epsilon_t} \left(\frac{\omega}{c}\right)^2, \quad \text{TM modes.} \tag{21}$$

By examining the dispersion relation of the whole system in (18), one can see that the dispersion characteristics have rotational symmetry for planes in wave vector space which are orthogonal to the k_z axis (xoy plane). This is why there is no difference in choosing k_y or k_x for dispersion analysis.

We can observe the dispersion characteristics of both the TE and TM modes in Fig. 7:

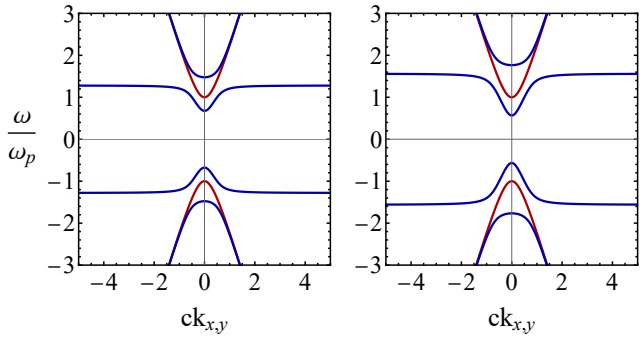

Fig. 7. Dispersion of the TM modes in blue and TE modes in red in the xoy plane for $\omega_c = 0.8\omega_p$ on the left, $\omega_c = 1.2\omega_p$ on the right and $\omega_p = 0.5c$ in both plots.

Since we are interested in computing gap Chern numbers, here follows a study of the existence of a full band gap between between the low-frequency TM band and the TE band (blue and red in Fig. 7, respectively). If we define the function for the amplitude of the band "gap" in question as $\omega_{gap}^1 = \widetilde{\omega}_H - \omega_L$, with ω_L as the limit of the TM bands when $k \to \infty$ and $\widetilde{\omega}_H$ as the lowest point of the TE branch:

$$\omega_L = \sqrt{\omega_c^2 + \omega_p^2}, \quad \widetilde{\omega}_H = \sqrt{\omega_p^2} = \omega_p, \tag{22}$$

we can then solve the inequality $\omega_{gap}^1 > 0$ to see if it is possible to get a full band gap.

$$\omega_{gap}^1 > 0 \Leftrightarrow \sqrt{\omega_p^2} > \sqrt{\omega_c^2 + \omega_p^2} \Rightarrow \omega_c^2 < 0 \tag{23}$$

There is no real valued ω_c that satisfies the inequality, thus there is no band gap between these two bands. This is a very relevant result for this work, since we can only apply the Green's function formalism to compute the gap Chern number for the low-frequency gap. It is to be noted that the TE modes also present reflection symmetry over both axes, and so there is no high-frequency band gap in the negative branches.

To work around the issue of an absent high-frequency band gap, we studied other models for the permittivity. A solution was achieved when shifting the plasma frequency as seen by the EM plane waves solely in the $\hat{\mathbf{z}}$ direction, and so we only change ϵ_z:

$$\frac{\epsilon_z}{\epsilon_0} = 1 - \frac{\omega_p'^2}{\omega^2}, \tag{24}$$

where $\omega_p' = \sqrt{K}\omega_p$ and K is a scalar. Considering that the only modes affected by this permittivity tensor component are the TE (20), for propagation in the xoy plane, we simply substitute ω_p in Eq. (22) with ω_p' which causes the modes to suffer a vertical shift. We study the possibility of a full band gap between this mode and the low-frequency TM mode, by redefining $\omega_{gap}^1 = \widetilde{\omega}_{H,K} - \omega_L$, with $\widetilde{\omega}_{H,K} = \omega_p'$ and so we need to find K that satisfies $\omega_{gap}^1 > 0$.

$$\omega_{gap} > 0 \Leftrightarrow \sqrt{K\omega_p^2} > \sqrt{\omega_c^2 + \omega_p^2} \Rightarrow K > \frac{\omega_c^2}{\omega_p^2} + 1 \tag{25}$$

The value of $\widetilde{\omega}_{H,K}$ must also be smaller than ω_H which is the lowest point of the high-frequency TM mode. This is because the longitudinal mode appearing along the k_z axis also suffers a shift with this new model, with dispersion $\omega = \omega_p'$. If this mode intersects the transverse modes that appear at higher frequencies, specifically at ω_H, with

$$\omega_H = \frac{\omega_c}{2} + \sqrt{\left(\frac{\omega_c}{2}\right)^2 + \omega_p^2}, \tag{26}$$

it could potentially alter the topology, which is not our objective. The constant must then be within an interval that depends only on the constitutive parameters ω_c and ω_p:

$$\frac{\omega_c^2}{\omega_p^2} + 1 < K < \frac{\omega_c^2}{2\omega_p^2} + \frac{\omega_c}{\omega_p^2}\sqrt{\left(\frac{\omega_c}{2}\right)^2 + \omega_p^2} + 1 \tag{27}$$

This slightly changed model has one crucial effect that is noticeable when looking at the dispersion in the k_z axis. For the regime $\omega_c < \omega_p$, the number of Weyl points is the same as with the original model, but in the regime $\omega_c > \omega_p$ the outer Weyl points no longer emerge in this system. This can be explained by analysing the low-frequency transverse modes propagating in the $\hat{\mathbf{z}}$ direction. When $k_z \to \infty$, the frequency of these modes will tend to a value $\omega \to \omega_c$ which, due to the plasma frequency shift, it is always smaller than ω_p'. Thus, this model only possesses one Weyl pair. Their location in momentum space is given by:

$$k_z^{Weyl} = \pm i\sqrt{\frac{\omega_p'(\omega_p^2 - \omega_c\omega_p' - \omega_p'^2)}{c^2(\omega_c + \omega_p')}} \tag{28}$$

The achieved high-frequency band gap in the xoy plane is highlighted in blue on the right plot of Fig. 8. We can see in the same plot that by shifting the TE band upwards it intersects the high-frequency TM band. This does not constitute a problem because it has been shown in [22] that the TE modes propagating in the xoy plane of a local magnetized plasma are topologically trivial. This means that this band's Chern number is zero, so even if this mode is shifted up due to the influence of ω_p', intersecting the high-frequency TM mode, the Chern number of the group formed by these two bands is equal to the Chern number of just the TM mode. This also means that

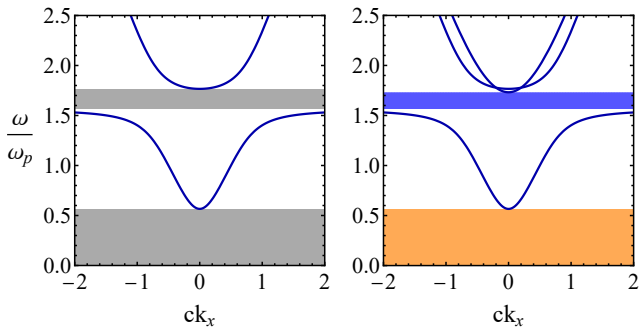

Fig. 8. Dispersion in xoy plane displaying only the TM modes on the left and both the TM and TE modes on the right, with the new ϵ_z. The band gaps are displayed in grey, blue and orange. TM modes are in blue and TE mode is in red. Parameters used on both plots were $\omega_c = 1.2\omega_p$ $\omega_p = 0.5c$. Plasma frequency shift on the right is given by $\omega_p' = \sqrt{2.8}\omega_p$.

this mode has a null contribution for the gap Chern numbers, ergo the high-frequency band gap of the right plot in Fig 8 is topologically equivalent to the band gap just between the TM modes. The latter is the high-frequency band gap observed in the left plot of Fig. 8. Furthermore the orange band gap is exactly the same as the low-frequency band gap in grey. The analytical results of the gap Chern numbers, for the band gaps depicted in this figure are presented in [8], [10], [22]. The gap Chern number of the high-frequency band gaps is $C^1_{gap} = +1$ and the low-frequency band gaps have a gap Chern number $C^2_{gap} = -1/\sqrt{1+\omega_p^2/\omega_c^2}$ which is not an integer far any non-zero ω_p.

The reason why the second gap Chern number is not an integer number is because the topology of the low-frequency TM mode is ill-defined, having a non-integer Chern number. Hence, an extra step is required. Since we are dealing with a continuous medium some cut-off should be included to the material response, so as to ensure that its nonreciprocal components are suppressed for large wave vectors.

B. Hydrodynamic Model

The hydrodynamic or drift-diffusion model of a magnetized plasma is an extension of the system described in the previous section, where the repulsive interactions between electrons are accounted for. The permittivity tensor ($k_z = 0$) of this model is:

$$\frac{\overline{\epsilon}_{hydro}}{\epsilon_0}(\omega,\mathbf{k}) = \mathbb{1} - \frac{\omega_p^2}{\omega^2}\left(\frac{\Delta}{\Delta+\omega_c^2}\mathbb{1}_t + \hat{\mathbf{z}}\otimes\hat{\mathbf{z}} - \frac{\beta^2\mathbf{k}\otimes\mathbf{k}}{\Delta+\omega_c^2}\right) + \frac{1}{\omega}\frac{i\omega_c\omega_p^2}{\Delta+\omega_c^2}\hat{\mathbf{z}}\times\mathbb{1}, \tag{29}$$

where β determines the strength of the diffusion due to charge concentration, $\Delta = \beta^2k^2 - \omega^2$, $k^2 = \mathbf{k}\cdot\mathbf{k}$, $\otimes$ is the tensor product and $\times$ is the cross product.

This model introduces spatial dispersion or nonlocality since the electric displacement and the electric fields are linked by differential operators, or in other words, the permittivity tensor depends on the wave vector $\mathbf{D} = \overline{\epsilon}(\omega,\mathbf{k})\cdot\mathbf{E}$, with $\mathbf{k} = -i\nabla$ (in the harmonic regime). The nonlocality only affects the longitudinal modes [10], [20]. For xoy propagation, the low frequency TM mode bends upward, so it no longer has the limit $\sqrt{\omega_c^2+\omega_p^2}$, but now $\omega\to\infty$ as $k\to\infty$. In the direction orthogonal to this plane, in the k_z axis, it is the longitudinal mode that gets curved, no longer staying flat and $\omega\to\infty$ as $k\to\infty$.

Similarly with the helical metamaterial case discussed in section II, the type of Weyl point changes with the introduction of the nonlocality. The crossings between the longitudinal mode and the transverse modes have isofrequency surfaces around it which are hyperboloids. This means that we are dealing with a type-II Weyl point, as one can observe in Fig. 9. This is analogous to the case of a negative α parameter in the helical metamaterial (see Fig. 3), and so we have a crossing between a longitudinal mode and a transverse mode, both with group velocities $v_g = \frac{\partial\omega}{\partial k}$ with the same sign.

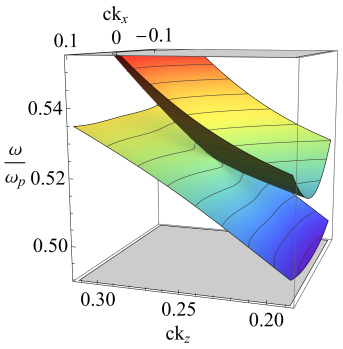

Fig. 9. Dispersion surfaces and isofrequency curves around Weyl point in **a)** $\hat{\mathbf{x}}$ and $\hat{\mathbf{y}}$ directions and in **b)** $\hat{\mathbf{z}}$ and $\hat{\mathbf{x}}$ directions. The parameters used here were $\beta = 0.6c$, $\omega_c = 0.2\omega_p$ and $\omega_p = 0.5c$.

With respect to the topological characterization of this model, there is one crucial effect that arises with this specific regularization procedure. The effect of the nonlocality on the low-frequency TM mode in the xoy plane prohibits the possibility of a high-frequency full band gap, even with a plasma frequency shift in the $\hat{\mathbf{z}}$ direction. Hence only the low-frequency band gap can be topologically characterized with our formalism.

C. Full Cut-off Model

The full cut-off model implements a high-frequency spatial cut-off to the material response of a system, as:

$$\overline{\epsilon}_{cut-off}(\omega,\mathbf{k}) = \epsilon_0\mathbb{1} + \frac{1}{1+k^2/k^2_{max}}\left(\overline{\epsilon}_{loc} - \epsilon_0\mathbb{1}\right), \tag{30}$$

where $\overline{\epsilon}_{loc}$ is the permittivity tensor of a local magnetized plasma, given by Eq. (14), but with ϵ_z given by Eq. (24). Just like the hydrodynamic model, the cut-off model of a magnetized plasma is spatially dispersive. However, the high-frequency material response is that of the vacuum and it is independent of the wave vector, i.e. local. Importantly, it becomes reciprocal because $\overline{\epsilon} = \overline{\epsilon}^T$.

The most significant effect is that the longitudinal mode in k_z axis bends downward, contrarily to the hydrodynamic model, and instead of being a flat mode its limit is set by $\omega \to 0$ as $k_z \to \infty$, for any real value of k_{max}. The immediate consequence is that for this model there are always two pairs of Weyl points in the k_z axis, because the longitudinal mode crosses two transverse modes.

The nonlocality also changes the type of Weyl point, but this time the isofrequency surfaces that surround the crossing are ellipsoids. Thus this model originates type-I Weyl degeneracies. We conclude that this is analogous to the case of a positive α parameter in the helical metamaterial (see Fig. 3). In these conditions, the group velocities of the longitudinal and transverse modes have different signs.

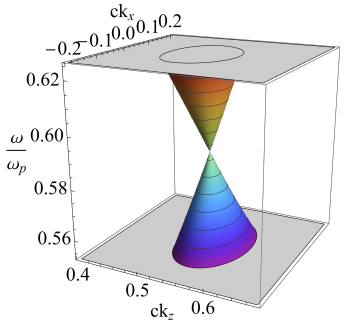

Fig. 10. Dispersion surface and isofrequency curves around Weyl point $\hat{\mathbf{z}}$ and $\hat{\mathbf{x}}$ directions. The parameters used here were $k_{max} = \omega_p/c$, $\omega_c = 1.2\omega_p$, $\omega_p' = \sqrt{3}\omega_p$ and $\omega_p = 0.5c$.

IV. Topological Study of Models With Regularized Responses

The first solution that we tried as a means to regularize the response of a magnetized plasma is the hydrodynamic model. For this study, we chose a set of constitutive parameters with which there is only one pair of Weyl points, and their location in momentum space will be referred to as $k_z = \pm W$ (plus sign for the one at a positive wave vector value and vice-versa). The two regions of interest are highlighted in blue and orange in Fig. 11. We can see a crucial consequence of this model in this figure. The longitudinal mode in the k_z axis lifts up, for any positive value of diffusion velocity β.

Additionally, in Fig. 12, the low-frequency TM mode in the k_x axis (for $k_z = 0$, top panel of the figure) also lifts up and this results in the nonexistence of a full band gap between the positive frequency modes, in any cross section at any k_z value. This makes it impossible to topologically characterize the blue region in Fig. 11. However, important results can be drawn from the topological study of the orange region. The two regions of interest are highlighted in blue and orange in Fig. 11.

Three cross sections were chosen with distinct k_z values: $k_z = 0$, $k_z = W$, $k_z = \frac{3}{2}W$, corresponding to a location in momentum space which is before, at and after the Weyl point, respectively. The band gaps that will be characterized are shown in Fig. 12. The gap Chern numbers computed for

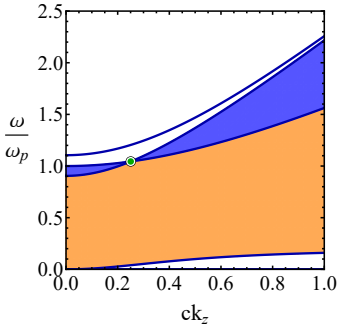

Fig. 11. Dispersion of the hydrodynamic model in the k_z axis exhibiting the two regions of interest in blue and orange. The Weyl crossing is highlighted with the green circle. The parameters used here were $\beta = 0.6c$, $\omega_c = 0.2\omega_p$, $\omega_p' = \omega_p$ and $\omega_p = 0.5c$.

the three cases were the same: $C_{gap} = 0$ which means that the three gaps are topologically trivial. This is expected for a combination of reasons. First of all, the orange region exhibits a full band gap in any cross section and for the interval $k_z \in]-\infty, +\infty[$, only the band gaps' amplitude varies and in a smooth way.

This means that, since there is no discontinuity, the gaps' topological invariants (in each cross section) should always be the same. Furthermore, as a result of the regularization, the material's nonreciprocal response for the low-frequency TM mode in the xoy plane is suppressed for large wave vectors, and specifically for $k \to \infty$ the medium is reciprocal which justifies the trivial topology.

The second solution to regularize the topology of a magnetized plasma is the implementation of a full spatial cut-off. With this model, two Weyl points always arise in the positive part of the dispersion characteristic, as observed in Fig. 13. The first or inner Weyl crossing appears for the wave vector value $k_z = W_1$ and the second or outer one appears for $k_z = W_2$. This solution is quite different from the hydrodynamic model, in the sense that we no longer have full band gaps in every cross section situated in the orange region. Specifically, the only values where a full band gap cannot be observed in the cross section are the outer Weyl points, $k_z = \pm W_2$. Additionally, with this model we can observe full band gaps in cross sections situated in the blue region as well. Again, the only values where no band gap is observed are the inner Weyl crossings, $k_z = \pm W_1$. As a consequence, we can topologically characterize two regions that are directly influenced by each Weyl point, by computing gap Chern numbers in cross sections before and after these crossings. The regions of interest are illustrated in Fig. 13. This time, various cross sections were considered in order to fully characterize both regions: $k_z = 0$, $k_z = \frac{3}{4}W_1$, $k_z = W_1$, $k_z = \frac{5}{4}W_1$, $k_z = W_2$ and $k_z = \frac{5}{4}W_2$. If we look at Fig. 14, we can see the high-frequency band gaps in blue are present except at the first Weyl crossing and the low-frequency band gaps in orange are present except at the second Weyl crossing. The gap Chern number C_{gap}^1 is relative to the blue region's band gaps and C_{gap}^2 is relative to the orange region's band gaps. For

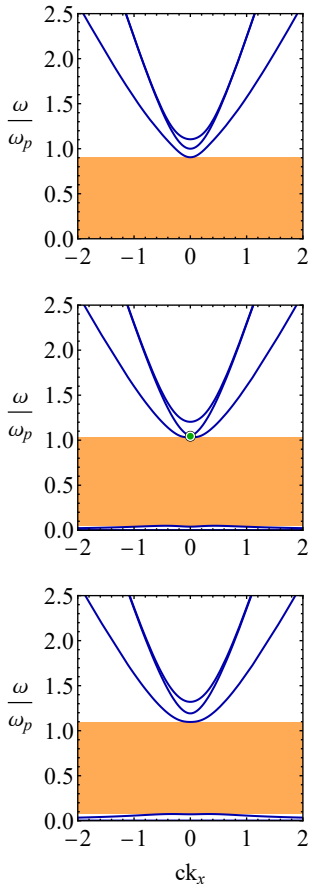

Fig. 12. Cross sections of the 3-dimensional dispersion of the hydrodynamic model for different values of k_z. From top to bottom, $k_z = 0$, $k_z = W$ and $k_z = \frac{3}{2}W$. The band gaps are highlighted in orange and the Weyl point with the green circle. The parameters used here were $\beta = 0.6c$, $\omega_c = 0.2\omega_p$, $\omega_p' = \omega_p$ and $\omega_p = 0.5c$.

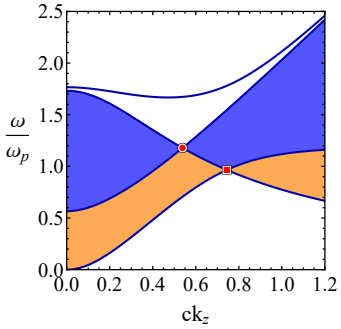

Fig. 13. Dispersion of the full cut-off model in the k_z axis exhibiting the two regions of interest in blue and orange. The parameters used here were $k_{max} = \omega_p/c$, $\omega_c = 1.2\omega_p$, $\omega_p' = \sqrt{3}\omega_p$ and $\omega_p = 0.5c$.

$|k_z| < W_1$, $C^1_{gap} = +1$ and for $|k_z| > W_1$, $C^1_{gap} = 0$, so we can clearly see an influence from the Weyl point. Specifically, the blue band gaps in cross sections between the negative and positive inner Weyl points are topologically non-trivial, and the blue band gaps beyond these values are topologically trivial. A similar result is observed for the low-frequency band gaps. For $|k_z| < W_2$, $C^2_{gap} = -1$, hence the orange band gaps in cross sections between the positive and negative outer Weyl points are topologically non-trivial, and they are trivial $C^2_{gap} = 0$ for $|k_z| > W_2$.

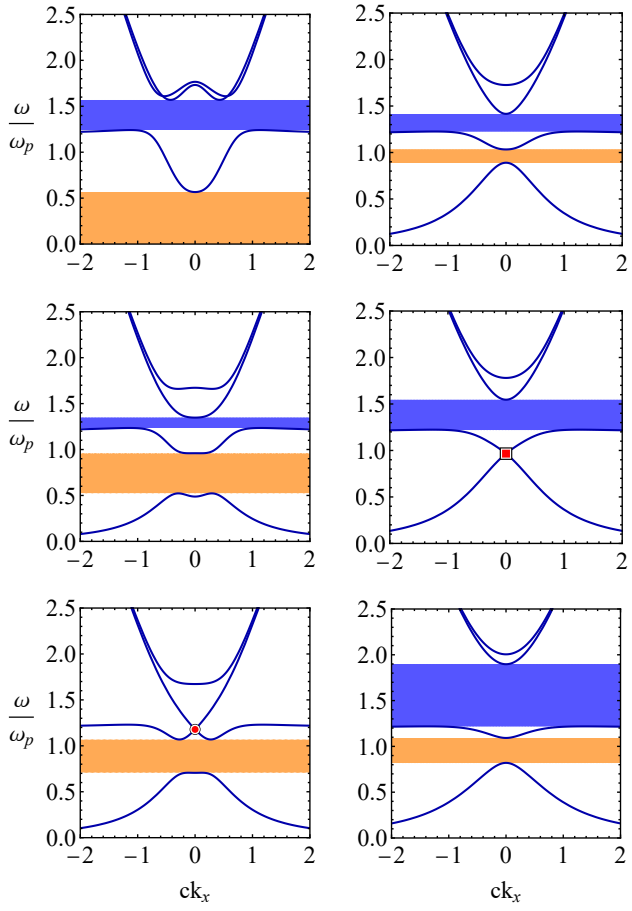

Fig. 14. Cross sections of the 3-dimensional dispersion of the full cut-off model for different k_z values. On the left, from top to bottom: $k_z = 0$, $k_z = \frac{3}{4}W_1$ and $k_z = W_1$. On the right, from top to bottom: $k_z = \frac{5}{4}W_1$, $k_z = W_2$ and $k_z = \frac{5}{4}W_2$. The high-frequency band gaps are highlighted in blue, the low-frequency ones in orange. The inner Weyl point is the red circle and the outer Weyl point is the red square. The parameters used here were $k_{max} = \omega_p/c$, $\omega_c = 1.2\omega_p$, $\omega_p' = \sqrt{3}\omega_p$ and $\omega_p = 0.5c$.

This corroborates the fact that the Weyl points are indeed sources and drains of Berry curvature, and so it is consistent with the emergence of the non-trivial topological properties in a magnetized plasma [13], because the cross section's band gaps in the regions confined between each pair were shown to be topologically non-trivial. It also explains why the orange band gaps of the hydrodynamic model are in turn trivial, since they are not confined between any pair of Weyl points.

Finally, to complete this study and to conclude the main objective of this thesis, we will quantify the Weyl points' monopole charge by computing the difference in the gap Chern numbers before and after the crossing, in a momentum space path across it. The sign can only be attributed by defining the

order in which the difference is computed. We will assume the negative orientation of the k_z axis as a convention to determine the order of the difference, which means that the minuend will be the gap Chern number in a cross section with a higher k_z than that of the subtrahend. The topological charge of the inner Weyl point with positive momentum is -1 since before the crossing, the gap Chern number is $C^1_{gap} = +1$ and after it is $C^1_{gap} = 0$. This is because the band gaps in the cross sections after the crossing are trivial, so the sum between C^1_{gap} before the crossing and the topological charge of the Weyl degeneracy should be zero. The outer Weyl point in the positive wave vector space has a topological charge of $+1$, since before the crossing the gap Chern number is $C^2_{gap} = -1$ and after it is $C^2_{gap} = 0$, by the same logic. The topological charge of the Weyl points that arise in the negative wave vector space have symmetric values since a pair of Weyl points constitute one source and one sink of Berry flux. The results are summarized in Fig. 15.

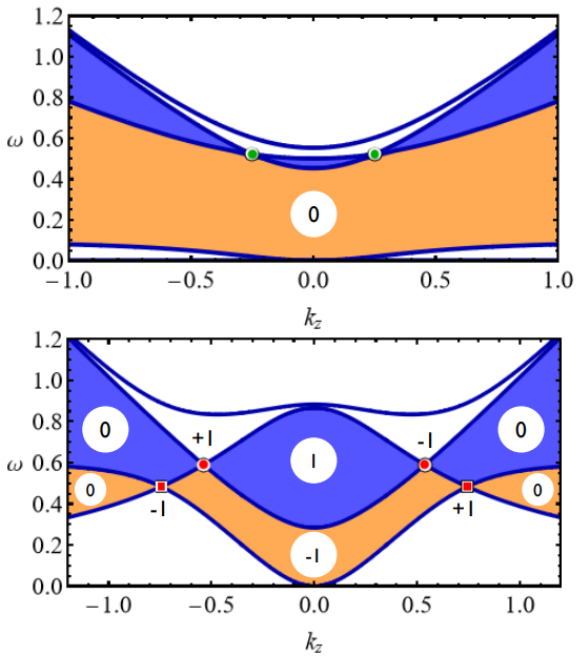

Fig. 15. The plot on top is the k_z axis dispersion of the hydrodynamic model with the Weyl pair as green circles. The plot on the bottom is the k_z axis dispersion of the cut-off model with the inner Weyl pair as red circles and the outer pair as red squares. The numbers in white circles represent the gap Chern numbers obtained in each region. Near the Weyl points of the cut-off model you can see the number that represents their topological charge. The parameters used for the hydrodynamic model were $\beta = 0.6c$, $\omega_c = 0.2\omega_p$, $\omega_p' = \omega_p$ and $\omega_p = 0.5c$ and the ones used for the full cut-off model were $k_{max} = \omega_p/c$, $\omega_c = 1.2\omega_p$, $\omega_p' = \sqrt{3}\omega_p$ and $\omega_p = 0.5c$.

V. Conclusions

To acquire Weyl points, it is necessary to break either time-reversal symmetry or inversion symmetry. The helical metamaterial has no inversion symmetry precisely because of the helical geometry, but this alone does not guarantee the twofold point-like degeneracies in the system. The permittivity components in the $\hat{\mathbf{x}}$ and $\hat{\mathbf{y}}$ directions (for a helix oriented along the $\hat{\mathbf{z}}$ direction) must also be different, or in other terms, the system's response must be anisotropic in planes that are orthogonal to the helix orientation. This is the reason why the unit cell has an elliptical helix.

In the case of the magnetized plasma, time-reversal symmetry is broken by the applied magnetic field. This is the reason why it is nonreciprocal which is a necessary property to obtain non-trivial topological invariants in this system [8], such as the gap Chern numbers. The existence of Weyl crossings in this medium is thus inherently connected with its nonreciprocity since they have been shown to be responsible for the non-trivial topological properties of the magnetized plasma [13]. This is corroborated by the results in section V of this dissertation.

The emergence of these Weyl degeneracies in both systems is similar, in the sense that the point-like band crossings occur along a single direction of propagation $\mathbf{k}$, between one longitudinal mode and transverse modes. Such direction is determined differently for each medium. It is given by the helices' principal axis for the helical metamaterial, and in the case of the magnetized plasma it is given by the direction of the static bias magnetic field.

The Weyl point generated by the crossing between a flat longitudinal mode and a transverse mode rests at the boundary between type-I and type-II. To acquire either type, nonlocality must be introduced into the system. If the nonlocality acts on the longitudinal mode by bending it upward (second derivative with respect to the wave vector is positive), the isofrequency curves around the crossing turn hyperbolic, thus it changes into a type-II Weyl point. If it bends downward (negative second derivative), the isofrequency curves turn into closed ellipses, thus changing it to a type-I Weyl point.

The introduction of spatial dispersion is a consequence of the regularization procedure for the local magnetized plasma. It was possible to replicate the two different types of Weyl crossings with the two solutions explored in sections III.A-III.B. On the other hand, the helical metamaterial possesses intrinsic strong spatial dispersion for any frequency and even in the very large wavelength limit [21]. By analysing the effective medium theory in [17], we showed that this nonlocality can only originate the second type.

The most important and novel conclusions were derived in section V, after the topological characterization of the band structures of two nonlocal models of a magnetized plasma. It was numerically shown that topologically non-trivial band gaps exist in specific regions of the 3-dimensional dispersion. These regions are confined between each Weyl point pair in momentum space. By taking cross sections of the dispersion in orthogonal directions ($k_{x,y}$) relatively to the axis that connects the pair (k_z) and if we can guarantee the existence of full band gaps in these cuts that are situated in the region of interest, we can compute their gap Chern number. Our results show that these band gaps are non-trivial. In fact, the gap Chern number remains constant for any cross section in this region. This is expected since the band gaps are all connected if we are looking along the k_z axis and they only change in amplitude

in an adiabatic way. The situation is completely different if we consider cross sections immediately before and after the Weyl crossing. As it was seen best in Fig. 15, the gap Chern numbers are different in each situation, becoming trivial in cross sections beyond the interval in wave vector space that directly connects the pair. This is also expected since the gaps in these cross sections are all connected even when $k_z \to \infty$, consequently the gap Chern number must be constant, and since in this limit the electromagnetic response is reciprocal, it should be indeed zero.

The previous arguments explain why the gap Chern numbers are trivial in cross sections situated in a region that is not bounded by any Weyl points, as is the case of the low-frequency (orange) region of the hydrodynamic model. Equivalently, since there are no Weyl crossings in this region, there is no Berry curvature flux being captured in the respective band gaps of the cross sections with our Green's function method.

The difference of the gap Chern numbers before and after the crossing is the magnitude of the topological charge of the Weyl point. However, the sign can only be attributed by defining the order in which the difference is computed. Such order is given by a trajectory with positive or negative orientation in the direction of the axis that unites the Weyl pair. This trajectory is defined before-hand as a convention and maintained for the computation of topological charges for all Weyl crossings. As we conclude in section V, for each pair with opposite wave vector values, there is one with a positive sign and another with a negative sign, representing the existence of a source and a drain of Berry flux. Our method can then quantify the magnitude of the topological charge and the relative signs between pairs (Fig. 15), but cannot distinguish which Weyl point has the positive or the negative charge out of each pair.

In conclusion, we have applied a first principles method to the calculation of topological charge of Weyl points in continuous media. Unlike standard methods based on the direct computation of the Berry curvature, this approach does not require the calculation of the eigenvectors at each value of the wave vector and is thus more computationally efficient. Future work may include analysing the topology of the helical metamaterial and study protected edge modes in these systems.

ACKNOWLEDGMENT

I wholeheartedly thank my supervisors for their patience and guidance all the way through the realization of this work. This work was supported by Fundação para a Ciência e a Tecnologia and Instituto de Telecomunicações under project HelicalMETA, UIDB/50008/2020.

REFERENCES

[1] T. Ozawa, H. M. Price, A. Amo, N. Goldman, M. Hafezi, L. Lu, M. C. Rechtsman, D. Schuster, J. Simon, O. Zilberberg, and I. Carusotto, "Topological photonics," *Rev. Mod. Phys.*, vol. 91, p. 015006, Mar 2019.

[2] M. S. Rider, S. J. Palmer, S. R. Pocock, X. Xiao, P. A. Huidobro, and V. Giannini, "A perspective on topological nanophotonics: Current status and future challenges," *J. Appl. Phys. 1*, vol. 125, p. 120901, Mar 2019.

[3] M. Kim, Z. Jacob, and J. Rho, "Recent advances in 2d, 3d and higher-order topological photonics," *Light: Science & Applications*, vol. 9, p. 130, jul 2020.

[4] S. Raghu and F. D. M. Haldane, "Analogs of quantum-hall-effect edge states in photonic crystals," *Phys. Rev. A*, vol. 78, p. 033834, Sep 2008.

[5] M. G. Silveirinha, "Bulk-edge correspondence for topological photonic continua," *Phys. Rev. B*, vol. 94, p. 205105, Nov 2016.

[6] M. G. Silveirinha, "Proof of the bulk-edge correspondence through a link between topological photonics and fluctuation-electrodynamics," *Phys. Rev. X*, vol. 9, p. 011037, Feb 2019.

[7] M. G. Silveirinha, "Topological theory of non-hermitian photonic systems," *Phys. Rev. B*, vol. 99, p. 125155, Mar 2019.

[8] M. G. Silveirinha, "Topological classification of chern-type insulators by means of the photonic green function," *Phys. Rev. B*, vol. 97, p. 115146, Mar 2018.

[9] F. R. Prudêncio and M. G. Silveirinha, "First principles calculation of topological invariants of non-hermitian photonic crystals," *Communications Physics*, vol. 3, p. 221, Dec 2020.

[10] M. G. Silveirinha, "Chern invariants for continuous media," *Phys. Rev. B*, vol. 92, p. 125153, Sep 2015.

[11] L. Lu, L. Fu, J. D. Joannopoulos, and M. Soljačić, "Weyl points and line nodes in gyroid photonic crystals," *Nature Photonics*, vol. 7, Apr 2013.

[12] M. Xiao, Q. Lin, and S. Fan, "Hyperbolic weyl point in reciprocal chiral metamaterials," *Phys. Rev. Lett.*, vol. 117, p. 057401, Jul 2016.

[13] W. Gao, B. Yang, M. Lawrence, F. Fang, B. Béri, and S. Zhang, "Photonic weyl degeneracies in magnetized plasma," *Nature Communications*, vol. 7, p. 12435, Aug 2016.

[14] B. Yang, Q. Guo, B. Tremain, L. E. Barr, W. Gao, H. Liu, B. Béri, Y. Xiang, D. Fan, A. P. Hibbins, and S. Zhang, "Direct observation of topological surface-state arcs in photonic metamaterials," *Nature Communications*, vol. 8, Jul 2017.

[15] D. Wang, B. Yang, W. Gao, H. Jia, Q. Yang, X. Chen, M. Wei, C. Liu, M. Navarro-Cía, J. Han, W. Zhang, and S. Zhang, "Photonic weyl points due to broken time-reversal symmetry in magnetized semiconductor," *Nature Physics*, vol. 15, Nov 2019.

[16] S. Howard, L. Jiao, Z. Wang, N. Morali, R. Batabyal, P. Kumar-Nag, N. Avraham, H. Beidenkopf, P. Vir, E. Liu, C. Shekhar, C. Felser, T. Hughes, and V. Madhavan, "Evidence for one-dimensional chiral edge states in a magnetic weyl semimetal co3sn2s2," *Nature Communications*, vol. 12, Jul 2021.

[17] M. G. Silveirinha, "Design of linear-to-circular polarization transformers made of long densely packed metallic helices," *IEEE Transactions on Antennas and Propagation*, vol. 56, no. 2, pp. 390–401, 2008.

[18] N. Engheta and R. W. Ziolkowski, *Metamaterials: Physics and Engineering Explorations*. John Wiley & Sons and IEEE Press, 2006.

[19] P. Huidobro, M. Silveirinha, E. Galiffi, and J. Pendry, "Homogenization theory of space-time metamaterials," *Phys. Rev. Applied*, vol. 16, p. 014044, Jul 2021.

[20] M. G. Silveirinha, "Nano-electromagnetics: Plasmonics and metamaterials," Dec 2019.

[21] P. A. Belov, R. Marqués, S. I. Maslovski, I. S. Nefedov, M. Silveirinha, C. R. Simovski, and S. A. Tretyakov, "Strong spatial dispersion in wire media in the very large wavelength limit," *Phys. Rev. B*, vol. 67, p. 113103, Mar 2003.

[22] M. G. Silveirinha, "Topological angular momentum and radiative heat transport in closed orbits," *Phys. Rev. B*, vol. 95, p. 115103, Mar 2017.